**Coated ZrN sphere-UO2 composites as surrogates for UN-UO2 accident tolerant fuels**

Costa, Diogo Ribeiro; Hedberg, Marcus; Adorno-Lopez, Denise; Delmas, Mathieu; Middleburgh, Simon; Wallenius, Janne; Olsson, Par

**Journal of Nuclear Materials**

[Cyswllt i'r cyhoeddiad / Link to publication](#)

28. Apr. 2024

# Coated ZrN sphere-UO$_2$ composites as surrogates for UN-UO$_2$ accident tolerant fuels

Diogo Ribeiro Costa [a,b], Marcus Hedberg [c], Denise Adorno Lopes [a,b], Mathieu Delmas [d],

Simon C. Middleburgh [e], Janne Wallenius [a], Pär Olsson [a]

[a] KTH Royal Institute of Technology, Nuclear Engineering, 106 91 Stockholm, Sweden

[b] Westinghouse Electric Sweden AB, 721 63 Västerås, Sweden

[c] Chalmers University of Technology, Nuclear Chemistry, 412 96 Göteborg, Sweden

[d] Archer Technicoat Ltd., High Wycombe, HP12 4JD, UK

[e] Bangor University, Nuclear Futures Institute, Bangor, Gwynedd, LL57 1UT, UK

## Abstract

Uranium nitride (UN) spheres embedded in uranium dioxide (UO$_2$) matrix is considered an innovative accident tolerant fuel (ATF). However, the interaction between UN and UO$_2$ restricts the applicability of such composite in light water reactors. A possibility to limit this interaction is to separate the two materials with a diffusion barrier that has a high melting point, high thermal conductivity, and reasonably low neutron cross-section. Recent density functional theory calculations and experimental results on interface interactions in UN-X-UO$_2$ systems (X = V, Nb, Ta, Cr, Mo, W) concluded that Mo and W are promising coating candidates. In this work, we develop and study different methods of coating ZrN spheres, used as a surrogate material for UN spheres: first, using Mo or W nanopowders (wet and binder); and second, using chemical vapour deposition (CVD) of W. ZrN-UO$_2$ composites containing 15 wt% of coated ZrN spheres were consolidated by spark plasma sintering (1773 K, 80 MPa) and characterised by SEM/FIB-EDS and EBSD. The results show dense Mo and W layers without interaction with UO$_2$. Wet and binder Mo methods provided coating layers of about 20 µm and 65 µm, respectively, while the binder and CVD of W methods layers of about 12 µm and 3 µm, respectively.

**Keywords:** accident tolerant fuel, UN-UO$_2$, coating technologies, surrogate composites.

1

## 1. Introduction

Uranium nitride (UN) is considered a promising accident tolerant fuel (ATF) candidate to substitute the standard $UO_2$ fuel in light water reactors (LWRs) or next generation reactor systems, primarily because of the compound's higher uranium density and thermal conductivity [1]. Nevertheless, the nitride fuel has a low oxidation resistance when in contact with the coolant water in the LWR system [2]. UN-$UO_2$ composites are proposed to overcome this drawback since the $UO_2$ phase would act as a protective barrier against UN oxidation [3]. However, previous studies demonstrate that the $UO_2$ and UN fuels interact during fabrication and form an undesired sesquinitride phase ($\alpha$-$U_2N_3$) [4,5,6]. Although it is possible to minimise the sesquinitride formation by tuning the sintering parameters [6], the UN-$UO_2$ composite system needs to be improved to eliminate this interaction, which is likely to worsen when the fuel is operated within a reactor.

A possibility to prevent this interaction is to coat the UN fuel with a material that has a high melting point, high thermal conductivity, and reasonably low neutron cross-section material. Based on recent studies on density functional theory (DFT) calculation [7] and experimental results on the interface interactions in UN-X-$UO_2$ systems (X = V, Nb, Ta, Cr, Mo, W) [8], molybdenum and tungsten are considered promising coating candidates for fabricating stable UN-$UO_2$ accident tolerant fuels. These studies aimed to provide both theoretical and experimental results to support the fabrication of an innovative ATF concept: coated UN spheres embedded in $UO_2$ matrix [9].

Different techniques are available to coat spheres with a dense and uniform layer. The most common methods are the atomic layer deposition (ALD) [10,11,12], physical vapour deposition (PVD) by magnetron sputtering [13,14,15,16,17], and chemical vapour deposition (CVD) [18,19,20]. But some adjustments are needed to coat spheres using these processes, including the use of a rotary drum coating vessel [16,17], a fluidised bed reactor [11], or even developing an entire sputtering reactor tool [15].

Alternatively, a method to coat spheres using micro-sized Mo [21,22] and W [23,24] powders is applied to fabricate ceramic-metallic (cermet) materials for Nuclear Thermal Propulsion (NTP) application. This method consists of mixing a polyethylene binder with either Mo or W powders and $UO_2$ microspheres, followed by consolidation of the mixtures to obtain the Mo/$UO_2$ or W/$UO_2$ cermets, respectively. The authors report the fabrication of high-density cermets (97.5-99.5 %TD) by SPS at 1673-2123 K and 50 MPa. Additionally, the

2

presented micrographs show a uniform distribution of $UO_2$ in the W [24] and Mo [22] metallic matrices. However, none of these studies used Mo and W nano-sized powders, which may provide an even better powder distribution around the spheres. Moreover, this simple, quick, inexpensive and potentially scalable coating method is not applied yet to coat UN spheres for UN-$UO_2$ composite ATF fabrication.

In this study, we present the processes used to fabricate coated ZrN sphere-$UO_2$ composites as surrogates for coated UN-$UO_2$ accident tolerant fuels. The decision to use ZrN spheres, instead of UN spheres, was made to reduce the generation of nuclear scrap during this development stage. Additionally, the spheres had an equivalent surface in comparison with the UN spheres used in our previous study [6]. Thus, the ZrN spheres were coated with Mo or W nanopowders by two different methods: i) using acetone as a dispersant for the Mo nanopowder; ii) using an organic binder to enhance the adherence of Mo or W onto the ZrN sphere surface. Afterwards, the Mo(wet)/ZrN, Mo(binder)/ZrN and W(binder)/ZrN coated spheres were pre-sintered at 1373 K for 1 h in Ar to provide interconnections between the coated nanoparticles, which minimised the powder removal during handling and transportation. Additionally, this pre-treatment was useful to eliminate the organic binder from the samples. The pre-sintered coated spheres (15 wt%) were mixed with $UO_{2.13}$ powder and consolidated by spark plasma sintering (SPS) at 1773 K and 80 MPa for 3 min in vacuum. These SPS parameters were selected based on the most severe sintering conditions used in our previous studies on uncoated UN-$UO_2$ composite fuels [6,25]. The pre-sintered coated spheres and the sintered composites were characterised by scanning electron microscopy (SEM) and energy dispersive X-ray spectroscopy (EDS) techniques.

This study also presents the results of chemical vapour deposition (CVD) of W onto the ZrN spheres as another W coating method. A composite fuel containing 15 wt% of W(CVD)/ZrN coated spheres in $UO_2$ was also fabricated by SPS, using the same parameters, and characterised by SEM-EDS coupled with a focused ion beam (FIB) and electron backscatter detector (EBSD). The findings from this study will be adapted to fabricate coated UN spheres-$UO_2$ composite fuels in our future work. Furthermore, these results may suggest new insights on using nanopowders and the CVD method as coating possibilities to manufacture new ATF concepts.

3

## 2. Methods

### 2.1 Raw materials

Uranium dioxide ($UO_2$) powder was provided by Westinghouse Electric Sweden AB, which had the following properties: O/U ratio of 2.13, fill density of 2.19 g/cm$^3$, specific surface area (B.E.T.) of 5.33 m$^2$/g, mean particle size of 20.2 μm, and 900 ppm of $H_2O$. More details about the $UO_{2.13}$ powder can be found in our previous articles [6,8,25].

ZrN microspheres were fabricated using a sol-gel method at Chalmers University of Technology [26]. The chemical compositions of the as-fabricated spheres were reported to be 5.3 ±0.1 wt% of carbon, 2.3 ±0.2 wt% of oxygen and 8.3 ±0.2 wt% of nitrogen, which give a chemical formula of $Zr(C_{0.5}O_{0.2})N_{0.6}$. The computed density of the spheres was about 50 %TD, considering geometric density measurements (average weight ~ 1.1 mg; average diameter ~ 850 μm). Henceforth in this work, the spheres are referred to as ZrN for brevity.

Tungsten (W, 99.95 %) and molybdenum (Mo, 99.9 %) nanopowders (US Research Nanomaterials, Inc.) were used as an alternative, suitable, inexpensive, and potentially scalable methodology for coating the microspheres.

### 2.2 Coating methods

#### 2.2.1 Powder coating

The ZrN spheres were coated with molybdenum or tungsten nanopowders using two different methods: wet and binder. The wet method used in this study for the Mo nanopowder was derived and optimised from our preliminary study [9], which consisted of i) dispersing the nanopowder in acetone under vigorous magnetic stirring for 30 min; ii) transferring this suspension (~10 mL) to another container with ZrN spheres; iii) evaporating the acetone and collecting the coated spheres; and iv) pre-consolidation of the coating layer by heat treatment of the Mo/ZrN spheres at 1373 K for 1 h in argon to improve the contact between Mo-Mo particles and Mo layer-ZrN spheres. This temperature was selected to favour only the initial sintering stage [27,28], i.e. the neck growth stage where each nanoparticle-nanoparticle contact enlarges without interaction with neighbouring nanoparticles [29]. Thus, the intermediate stage of sintering, where neighbouring necks grow and interact with each other to form a network of tubular pores [27,28,29,30,31], did not occur.

4

A method to coat the spheres with Mo or W using a binder agent (Shell Omala S2 G320) was developed in order to improve the adherence of the nanopowders onto the spheres. It was previously demonstrated [9] that W nanopowder did not adhere well on the spheres by only using the wet method. In the binder procedure, the spheres were mixed with the binder using a small beaker (25 mL) and spatula, followed by the addition of either Mo or W nanopowders. The Mo/ZrN and W/ZrN coated spheres were also heat treated at 1373 K for 1 h in argon to pre-sinter the coating layer, as well as to eliminate the organic binder at moderate temperatures (>773 K).

### 2.2.2 Chemical vapour deposition

Chemical vapour deposition (CVD) of W was also used as a coating method. In this process [32,33,34], the spheres were loaded in a clean alumina boat and placed into the chamber of a CVD reactor specially designed at Archer Technicoat Ltd. for W coatings. This process used tungsten hexafluoride ($WF_6$) and hydrogen as reactive gases to deposit W metal onto the sphere surface ($H_2/WF_6$ pressure ratio of 15/1). The chamber was evacuated and maintained at a pressure below 10 mbar, while an argon flow (BOC, 99.995%) was established. The chamber was heated up to 623 K and, when the system temperature was considered stable, the argon flow was replaced by a mixture of $WF_6$ (Versum Materials, 99.9%) and $H_2$ (BOC, 99.99%). After the reaction period (30 min), the $WF_6$ flow was stopped, leaving the system to purge under pure hydrogen for 20 min. The hydrogen was subsequently replaced by argon for 20 min. At the end of the purge, the furnace was turned off, and the reaction chamber was filled with argon and left to cool down to ambient temperature.

### 2.3 Composite fuel fabrication

Composite fuels containing about 15 wt% of (uncoated) ZrN, Mo(wet)/ZrN, Mo(binder)/ZrN, W(binder)/ZrN or W(CVD)/ZrN spheres in $UO_2$ were fabricated by the spark plasma sintering (SPS) method at the National SPS Facility in Stockholm/Sweden. This sintering technology is a field-assisted process that uses low voltage and high current, combined with applied pressure, to consolidate powders [35,36]. The spheres were manually mixed with the $UO_{2.13}$ powder in a beaker using a spatula, and then poured out in a graphite die (9.5 mm inner diameter), all carried out within an argon-filled glovebox (< 0.1 ppm $O_2$) connected to the SPS machine. The SPS chamber was depressurised to about 5 Pa to sinter the

5

samples at 1773 K and 80 MPa, using the following thermal profile: heating at 100 K/min until 1573 K and then 50 K/min until 1773 K, held at this plateau for 3 min and cooled to 1173 K at 50 K/min. From 1173 K until room temperature, the system was cooled naturally (furnace inertia). More details about the SPS machine and sintering procedures can be found in our previous studies [6,25].

*2.4 Characterisation of the coated spheres and composites*

The morphology of the (unmounted) ZrN and all pre-sintered coated-ZrN samples were assessed by SEM, using an accelerating voltage of 7 kV and secondary electron (SE) detector. Additionally, qualitative EDS examinations were carried out to assess the distribution of the chemical elements in each sample. The SEM/FIB used for this purpose was a field emission gun SEM FEI Nova 200 Dual-Beam with EDS detector Aztec Ultim (Oxford Instruments) and a Ga ion beam source.

All coated and pre-sintered spheres were hot-mounted in a phenolic resin with carbon filler to examine their cross-sections. However, the W and Mo layers coated with nanopowders were removed during the grinding step, since the nanoparticles were only weakly connected. So, only the W(CVD)/ZrN regular cross-section is reported in this study. In addition, a FIB cross-section was performed in the unmounted W(CVD)/ZrN sample to evaluate the W coating layer and the W-ZrN interface. This FIB cross-section analysis was important to examine a fresh coating layer and interface, thus reducing the influence of any defect originated during regular sample preparation (cutting, grinding, polishing) [8].

EBSD analysis was performed at the W layer in the mounted W(CVD)/ZrN sample to evaluate the W grain morphology, size and orientation. Before the EBSD examination, the same polished cross-section used for SEM-EDS characterisation was last polished using an alumina ($Al_2O_3$) suspension (Buehler MasterPrep, 0.05 μm) for 20 min. The examination was carried out using an SEM JEOL 7800F equipped with a Bruker's e-Flash EBSD detector.

The sintered X/ZrN-$UO_2$ composites (X = Mo, W) were cut radially and hot-mounted in the same resin for standard metallographic preparation (grinding and polishing). All polished cross-sections were coated with carbon and examined by SEM-EDS in the same SEM equipment.

**3. Results and discussion**

6

## 3.1 Morphology of the materials

Fig. 1 reports the morphologies of the as-fabricated ZrN spheres and the Mo and W nanopowders used to coat the spheres. The spheres have a porous and cracked surface. However, the ZrN spheres have an equivalent surface area in comparison with the UN spheres (similar diameters). Since these spheres were used as a surrogate for the UN spheres, aiming only to reduce nuclear scrap during this current development stage, we have decided to use the ZrN spheres as received even though they were not dense nor high purity. The Mo nanopowder had spherical nanoparticles (~ 25-90 nm) and small agglomerates (~ 200-1200 nm), characteristic of Mo nanopowders [28,37,38]. The W nanopowder had an acicular-like morphology with an aspect ratio of ~2.5 (~ 150 x 60 nm) and larger agglomerates (~3000 nm). The same tendency of forming agglomerates is observed in previous studies [31,39].
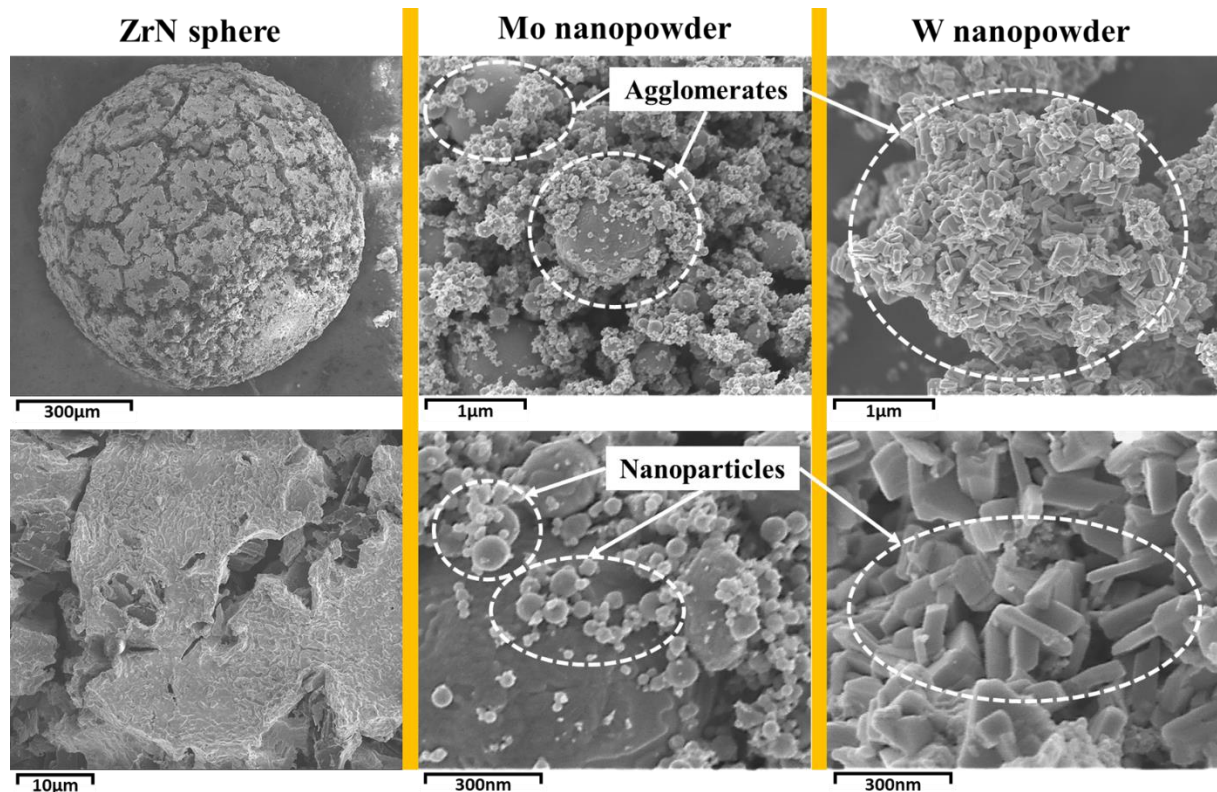


**Fig. 1.** SEM-SE images of ZrN spheres and Mo and W nanopowders. The spheres had an average diameter of ~ 850 μm and a density of ~50 %TD. Mo nanopowder had spherical nanoparticles (25-90 nm) and small agglomerates (200-1200 nm). W nanopowder nanoparticles were ~ 150 x 60 nm (aspect ratio of ~2.5) with larger agglomerates (~ 3000 μm).

## 3.2 Morphology and chemical composition distribution of the coated spheres

7

Fig. 2 reports the morphology of all (unmounted) coated ZrN spheres after pre-sintering and CVD. Regarding the Mo coating, the wet method provided a smoother surface with the nanoparticles connected by the necks formed between particles during the pre-sintering step [27,28,29,30,31]. The spheres coated by the binder method also presented connected particles but with a rougher surface. Conversely, the W(binder)/ZrN sample had a smother surface than Mo(binder)/ZrN. The CVD method provided the smoothest and densest coating layer.

The morphologies of the pre-sintered Mo(wet)/ZrN and Mo(binder)/ZrN samples in Fig. 2 are similar to those presented in a previous study on sintering Mo nanopowders in $H_2$ [28]. In the study, the authors report that a quenched micrograph of a sample sintered at 1273 K had a density of ~53 %TD, with the microstructure corresponding to the initial-stage sintering. Another study shows similar microstructures of Mo compacts sintered by SPS at 1273 K (~ 65 %TD) and 1373 K (~75 %TD) in $H_2$ [40]. Tungsten powder sintered at 1473 K by conventional sintering (68 %TD) and SPS (67 %TD) in vacuum also had a porous structure with agglomerates [30]. Similar surface morphology and dense W layer by CVD are observed in previous articles [41,42,43].
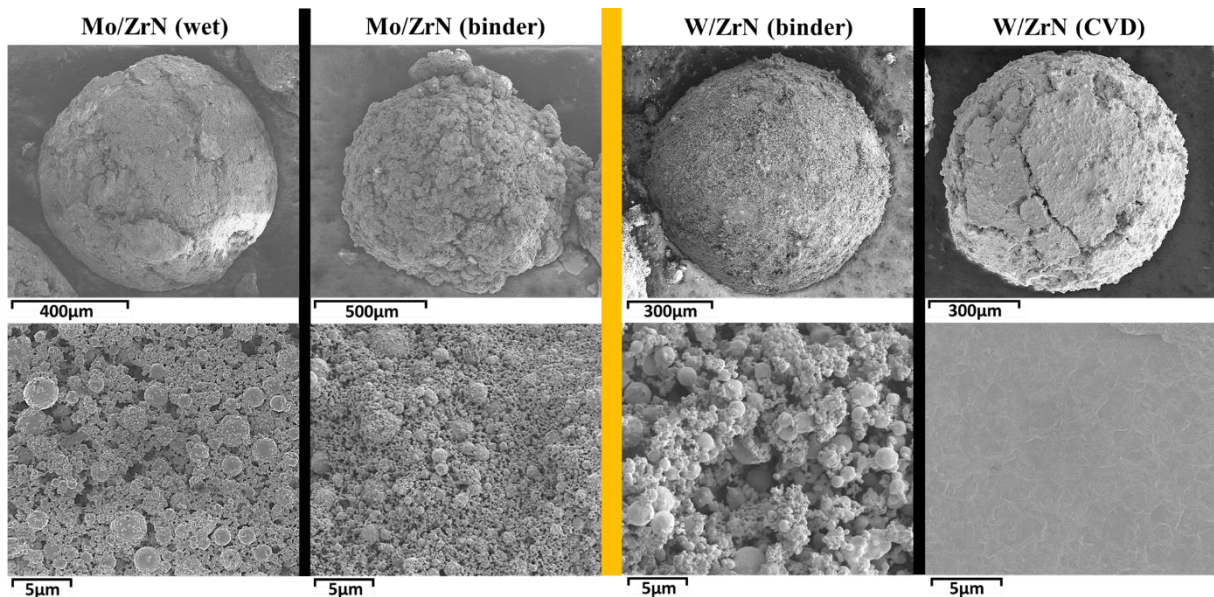


**Fig. 2.** SEM-SE images of the (unmounted) coated spheres after pre-sintered at 1373 K for 1 h in Ar. The samples coated by the wet and binder methods had porous structures with particles connected by necks formed during the initial stage of sintering [29]), similarly to observed in previous studies [28,30,40,42,43]. The CVD method provided a surface with the smoothest and densest coating layer, which is characteristic of this method [41,42,43].

8

The distributions of the chemical elements over the external surface of each (unmounted) coated sphere are shown in Fig. 3. Zr-rich regions in the EDS mapping may indicate either a thin coating layer (a few hundreds of nanometres), porous regions, or a lack of coating material in a specific region. In the Mo(wet)/ZrN sample, Zr-rich regions are observed on some cracks. The EDS map of O followed the same pattern, indicating that some regions were not completely coated or the layer was thinner than the interaction volume of the incident electron beam during the mapping [44]. Carbon-rich regions, related to impurity ingress from the ZrN sphere synthesis, are also observed in the maps. The EDS maps of Mo(binder)/ZrN presented fewer Zr- and O-rich regions, which may be the result of a thicker and rougher coating layer. The distribution of Zr and O over W(binder)/ZrN may indicate a thin coating layer on those regions. A uniform and dense layer of W was obtained by CVD, as observed by the absence of Zr-rich regions in the map. Thus, the CVD method seems to cover the whole sphere, including the open pores and cracks by infiltration of the reactants, as reported by other authors [34,45].
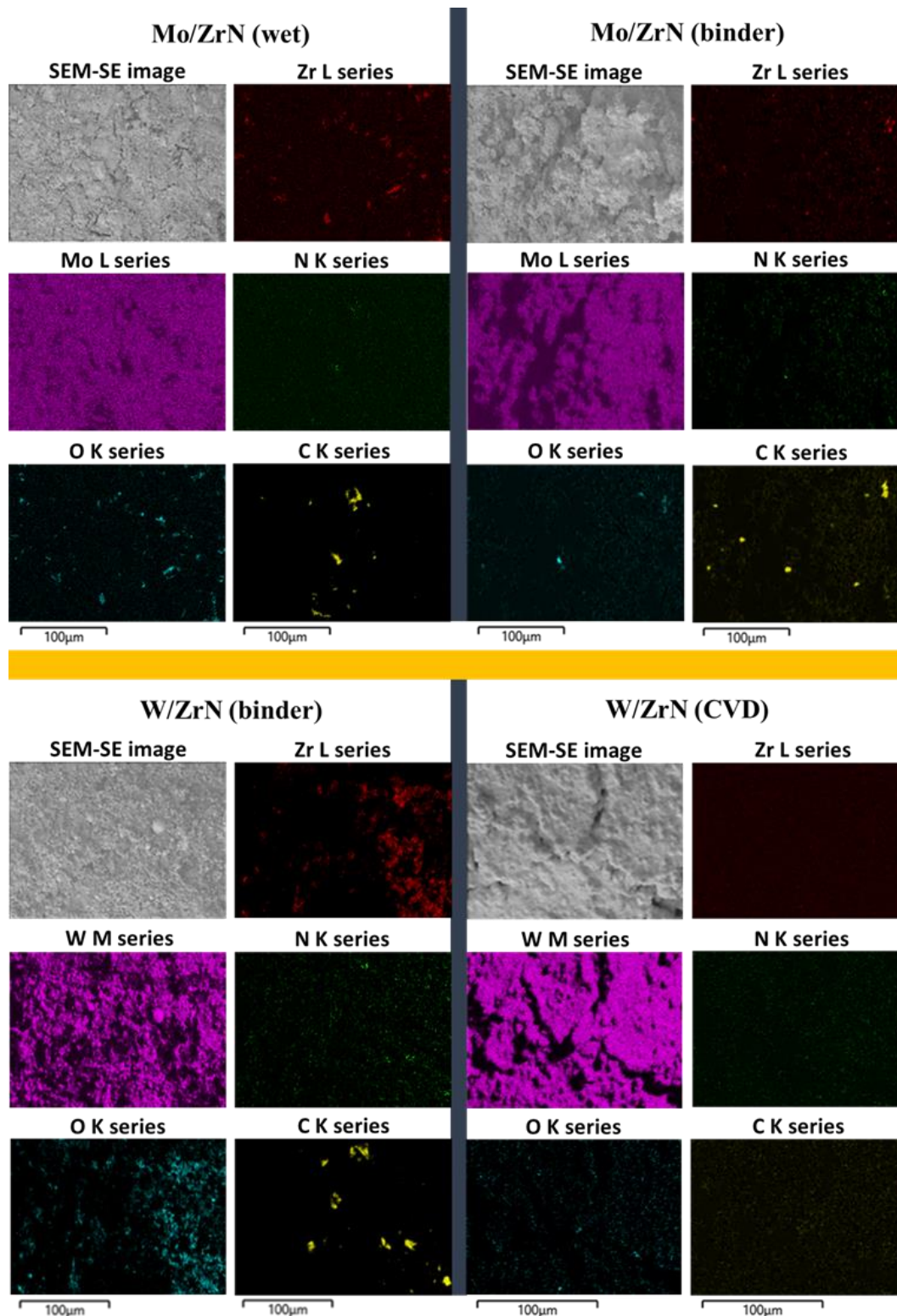
**Fig. 3.** SEM-EDS maps on the external surfaces of (unmounted) coated ZrN spheres. Zr-rich regions are observed in all samples, except in W(CVD)/ZrN. This may indicate either a lack of coating material of a thin coated layer in the samples coated with nanopowders [44].

Fig. 4 presents a FIB cross-section of an unmounted CVD-coated sphere to evaluate a fresh interface, without the addition of defects possibly generated during standard sample preparation (cutting, grinding, polishing) [8]. The EDS mapping of W shows a dense and ~3-µm thick layer that infiltrated the available open porosity (also observed in Fig. 5). The EDS map of F shows that fluorine was trapped in the pores and the inner region of the W layer (near the ZrN surface, at the W/ZrN interface). The ZrN surface roughness, as seen in Fig. 1, might have contributed to trapping of the fluorine during the growth of the W layer by the CVD process. This contamination needs significant attention as this may contribute to pellet-cladding interaction (PCI) and stress corrosion cracking (SCC) in a real fuel [46].

Previous studies report different CVD-W layer growth based on different substrate materials and surface morphologies [19,20,41,47]. So, a smoother substrate surface, combined with some changes in the CVD coating parameters, may minimise the infiltration and trapping of F in the sample and inner layer. It is reported that the infiltration process depends on the $H_2$ pressure; the lower the pressure, the more significant is the infiltration of F. However, the $H_2$ pressure has to be (at least) three times the $WF_6$ pressure to guarantee the reaction stoichiometry and provide W growth on the substrate. Thus, by increasing the $H_2/WF_6$ pressure ratio, the conditions for hydrogen chemisorption are favoured and the saturation of the substrate surface with adsorbed fluorine is avoided due to HF formation [32,45,48].



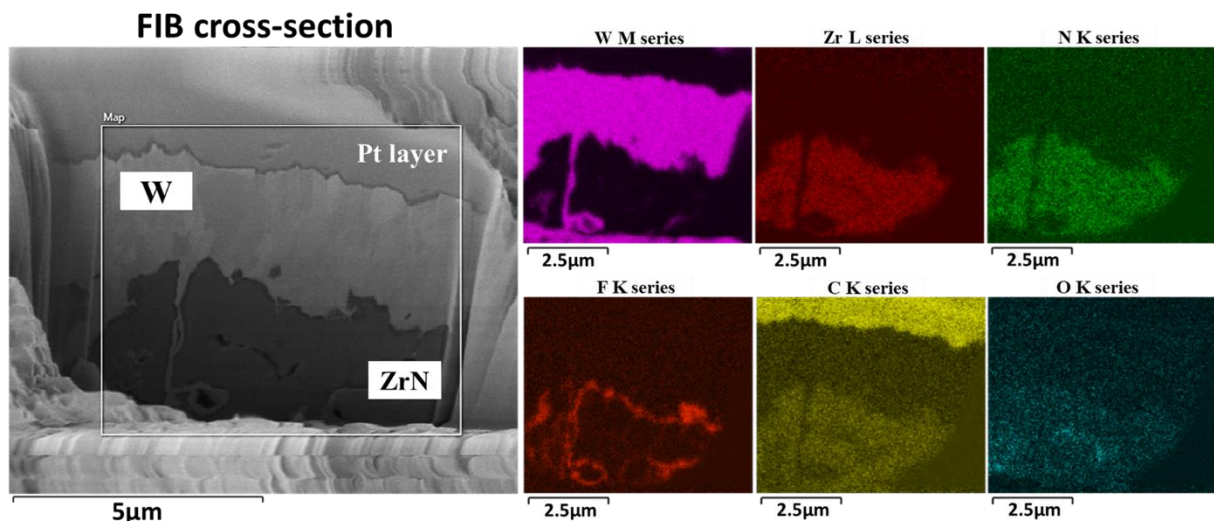**Fig. 4.** SEM-EDS mapping of a FIB cross-section of an unmounted W(CVD)/ZrN sphere. The EDS map of W shows a dense and ~3-µm thick layer that infiltrated via open porosity. The EDS map of F shows that fluorine was trapped in the pores and the inner region of the W layer.

11

The regular cross-section and EDS mapping of W(CVD)/ZrN in Fig. 5 shows a dense and well-adhered W layer, even after the mechanical grinding and polishing steps for sample characterisation. An average W thickness of $3.3 \pm 0.4$ μm was computed after 230 thickness measurements in five mounted W(CVD)/ZrN spheres. The W layer morphology and thickness portrayed in Fig. 5 match those observed in the FIB cross-section (Fig. 4). As such, regular cross-sections can be used to characterise coated spheres without losing their structural and chemical characteristics.

The W chemical map in Fig. 5 shows the high purity and density of the deposited W layer. The traces of C and O inside the sphere were from ZrN impurities (fabrication process), while the F content was due to infiltration and trapping of F in the ZrN pores at the beginning of the deposition step. This infiltration process, also known as chemical vapour infiltration (CVI) [49], is a desired output in some applications. For instance, to fabricate tungsten fibre-reinforced tungsten ($W_f$/W) composites for the first wall and armour material for future fusion devices [45,48]. As discussed above, this infiltration process is characteristic of CVD-W in porous materials [34] and can be minimised by using smoother and crack-free substrates (e.g. denser UN spheres), as well as by tuning some parameters during the CVD process (e.g. $H_2$/$WF_6$ pressure ratio) [32,34,45,48].
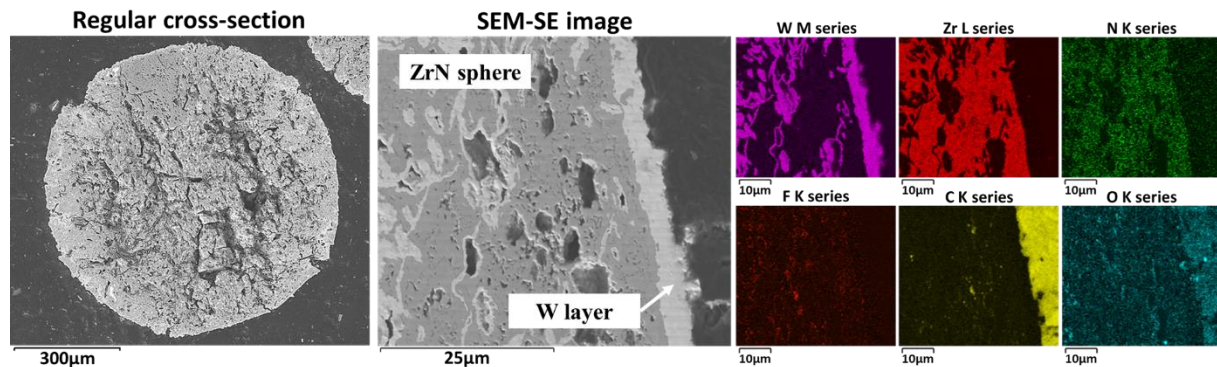


**Fig. 5.** SEM-EDS maps of a regular cross-section of W(CVD)/ZrN. W map shows the high purity and density of the deposited W layer. The presence of W and F inside the sphere was due to infiltration of the reactants during CVD, characteristic of porous materials [34,45,48].

The EBSD result of W(CVD)/ZrN in Fig. 6 shows polycrystalline W grains with (mostly) a columnar structure, i.e. grain growth occurring perpendicular to the substrate surface. The computed average grain size was approximately 0.6 μm, with minimum and

maximum values of ~ 0.2 μm and ~ 1.6 μm, respectively. The inverse pole figure (IPF) reveals no preferred crystallographic grain orientation, with approximately 33%, 28% and 39% of the grains oriented on the <111>, <001> and <101> directions, respectively.

Previous results also report a columnar grain structure of CVD-W [34,42,43,41,47,50,51], while others reported fine-grained or equiaxed grain structures [52,53]. Different preferential grain growths are reported along <100> [51], <101> [41] and <110> [47]. These differences demonstrate that temperature, pressure, gas flow, and substrate affect the thermodynamics and kinetics in the CVD growth [19,20]. Thus, the grain structures, sizes and orientations presented in Fig. 6 may slightly differ from what can be expected from our future work on CVD-W onto UN spheres, since those spheres are made of different materials and have different morphology (surface roughness, open porosity, and density).



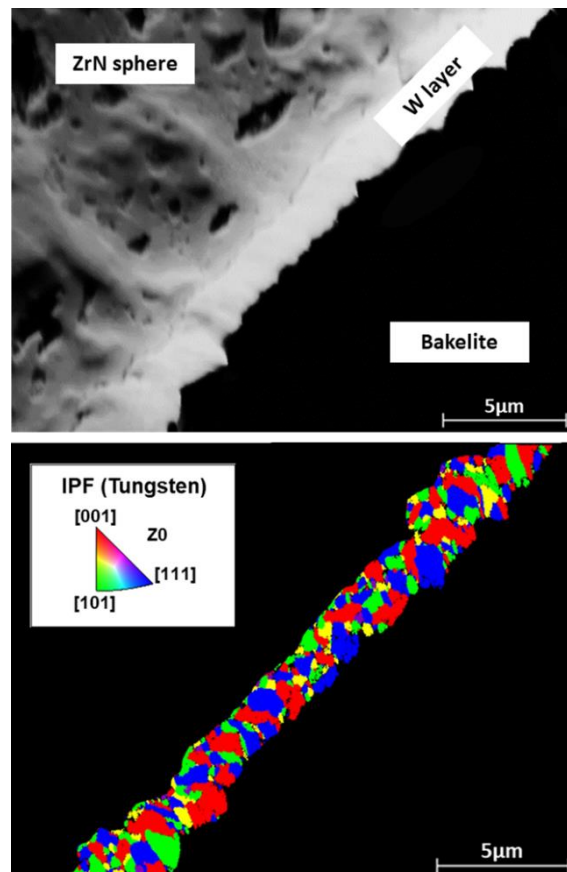**Fig. 6.** EBSD characterisation of the W layer of the mounted W(CVD)/ZrN sample. Polycrystalline W grains with (mostly) columnar structures are observed, with is in agreement with previous results [34,42,43,41,47,50,51]. The computed average, minimum and maximum grain sizes were approximately 0.6 μm, 0.2 μm and 1.6 μm, respectively. The inverse pole figure (IPF) reveals no preferred crystallographic grain orientation.

13

*3.3 Composite fuel microstructures*

*3.3.1 ZrN-UO$_2$ composite*

Fig. 7 shows the microstructure and EDS mapping of the uncoated ZrN-UO$_2$ composite. The SEM images of the embedded ZrN spheres in UO$_2$ shows some spheres surrounded by a dense UO$_2$ matrix. No interaction was observed between ZrN and UO$_2$, as evidenced by the EDS maps of U, Zr, O and N. This behaviour was expected since ZrN is chemically stable under different conditions, such as a diffusion barrier against interactions between dispersed U-Mo fuel particles and the surrounding Al matrix [15,54,55,56]. Additionally, ZrN can act as a protective layer against oxidation of AISI 304 stainless steel (304SS) [57] and as a coating material to improve the durability of cemented carbide (YT15, WC + 14 wt% TiC + 6 wt% Co) under aggressive environments [58]. Thus, ZrN may also be a good coating option to protect UN spheres against interaction with UO$_2$. However, it is pertinent to mention that the ZrN coating can interact with, for instance, the Al matrix under irradiation [59]. Thus, the coating thickness is crucial due to possible interactions between ZrN-UN and ZrN-UO$_2$ under irradiation.



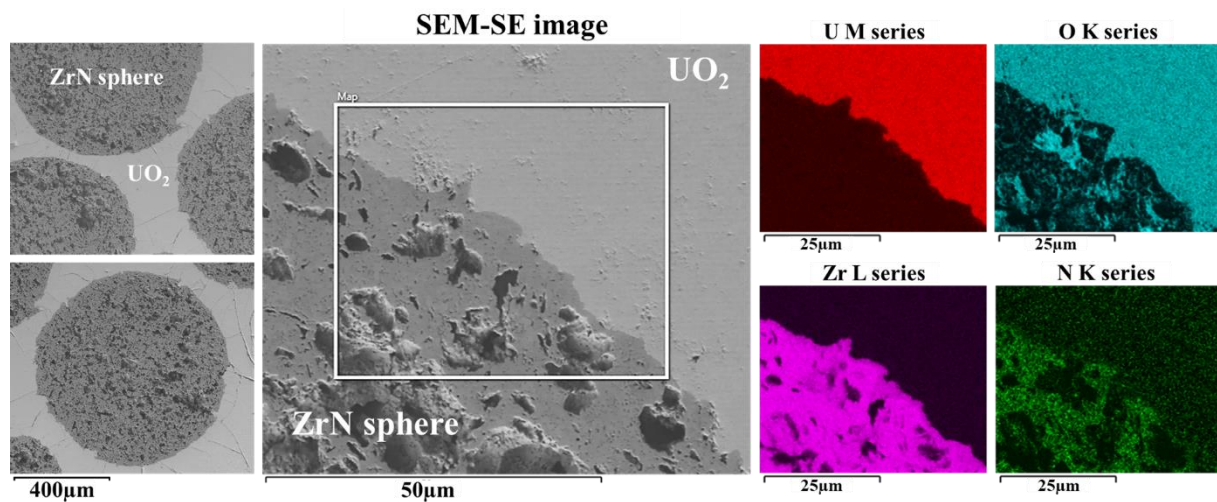**Fig. 7.** SEM-SE images of ZrN spheres embedded in UO$_2$ matrix and an EDS mapping at the ZrN-UO$_2$ interface. The ZrN spheres were surrounded by a dense UO$_2$ matrix without interacting with UO$_2$, as evidenced by the EDS maps of U, Zr, O and N.

*3.3.2 Mo/ZrN-UO$_2$ composites*

Fig. 8 reports the SEM images and EDS mapping of the Mo(wet)/ZrN-UO$_2$ sample. The composite had a cracked UO$_2$ matrix with a dense Mo layer and a sharp interface between Mo and UO$_2$. The cracks observed in the UO$_2$ matrix may be due to thermal expansion mismatch between Mo/ZrN and UO$_2$, which can develop residual stress during cooling [60]. At the sintering temperature (1773 K), for instance, the linear thermal expansion coefficient (α) of the UO$_2$ matrix [61] is approximately 50 % greater than that of the embedded Mo/ZrN spheres [62,63]. Thus, during the cooling step (50 K/h), the UO$_2$ phase tended to shrink faster than the coated spheres and, consequently, undergoes tensile stresses. Since ceramic materials are, in general, more brittle under tensile stress than under compressive stress [60], the coated spheres (which suffered compressive stresses) maintained their structure and did not crack, while the UO$_2$ matrix did. Similar crack behaviour is also reported in previous studies on UO$_2$-Mo systems [22,64,65,66]. These results demonstrated that the Mo coating layer resisted the most severe sintering conditions (1773 K, 80 MPa) we have used to fabricate uncoated UN-UO$_2$ composites [6].

The EDS mapping (matrix) in Fig. 8 shows that the spheres were covered with a Mo layer o f about 20 μm (average), with the thicker regions located at the porosity and cracks on the surface. At the interface (bottom), the Mo chemical map shows that the nanoparticles filled the pores and cracked regions. Moreover, the Mo and O maps demonstrate that the Mo nanoparticles sintered and became a dense Mo layer with no interaction with the UO$_2$ phase. This result agrees with our previous article on pressure-assisted diffusion experiment in UN-Mo-UO$_2$ composite [8], which indicates that a coating layer of ~500 nm would be enough to protect the UN against interaction with UO$_2$ during manufacture. This protection is sufficient to avoid the interaction during fabrication but does not consider the irradiation-induced diffusion of both oxygen and nitrogen. Further experimental and modelling studies are needed to evaluate the effect of irradiation on the diffusion behaviours of O and N in the coated UN-UO$_2$ systems.
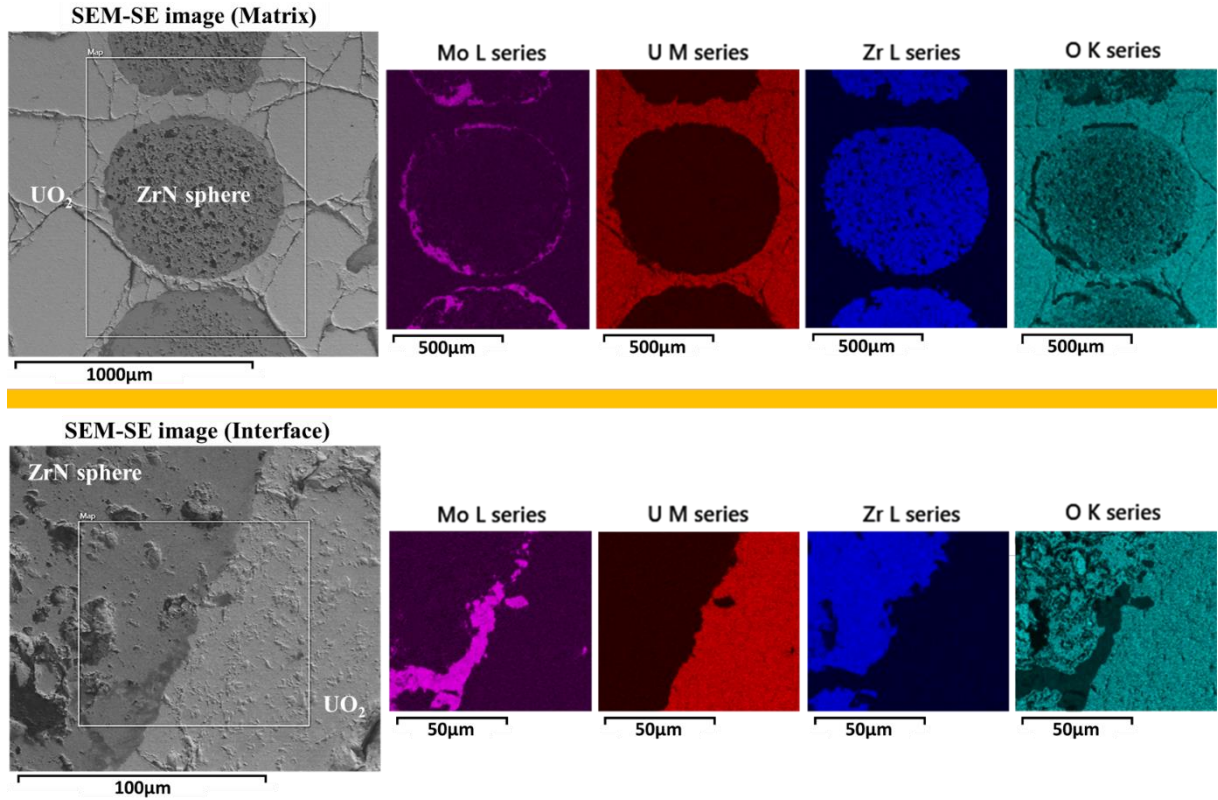
15

**Fig. 8.** SEM-EDS images of the Mo(wet)/ZrN-UO$_2$ composite showing the coated spheres embedded in the UO$_2$ matrix (top) and the ZrN-Mo-UO$_2$ interface (bottom). The composite had a cracked UO$_2$ matrix with a Mo layer (~ 20μm) covering the spheres. The EDS maps (bottom) of Mo and O reported no interaction between the materials, which agrees with our previous article on pressure-assisted diffusion experiment in UN-Mo-UO$_2$ composite [8].

The EDS maps of the Mo(binder)/ZrN-UO$_2$ composite are presented in Fig. 9. This coating method provided a thicker Mo layer (~65 μm) than the wet method (~ 20 μm). Additionally, no C contamination from the binder agent is observed in the coating layer. As reported in the wet method (Fig. 8), the UO$_2$ matrix cracked, and the Mo layer was dense and effective to avoid O migration from the UO$_{2.13}$ precursor powder towards the nitride phase. The denser structure of Mo observed in the bottom figure, compared with the starting condition in Fig. 2, confirms that the nanopowder sintered during the composite fabrication. A previous study on SPS of Mo nanopowder reports a sintered density of about 95 %TD at 1773 K [28]. Moreover, it is shown [37] that the relative density of Mo varied from 58 %TD (at 1123 K, 67 MPa) to 95 %TD (at 1873 K, 67 MPa) during SPS (i.e. both open and closed porosity). So, from previous results [27,28,37,40], it seems that the Mo nanopowder started sintering at ~1273 K and drastically increased its density up to ~ 1473 K during SPS, where the shrinkage ends and the final sintered density (> 95 %TD) is (almost) achieved. Improvements in this

16

method are needed to obtain a thinner, smoother, and more uniform Mo layer, which would be more beneficial to the neutronic performance.
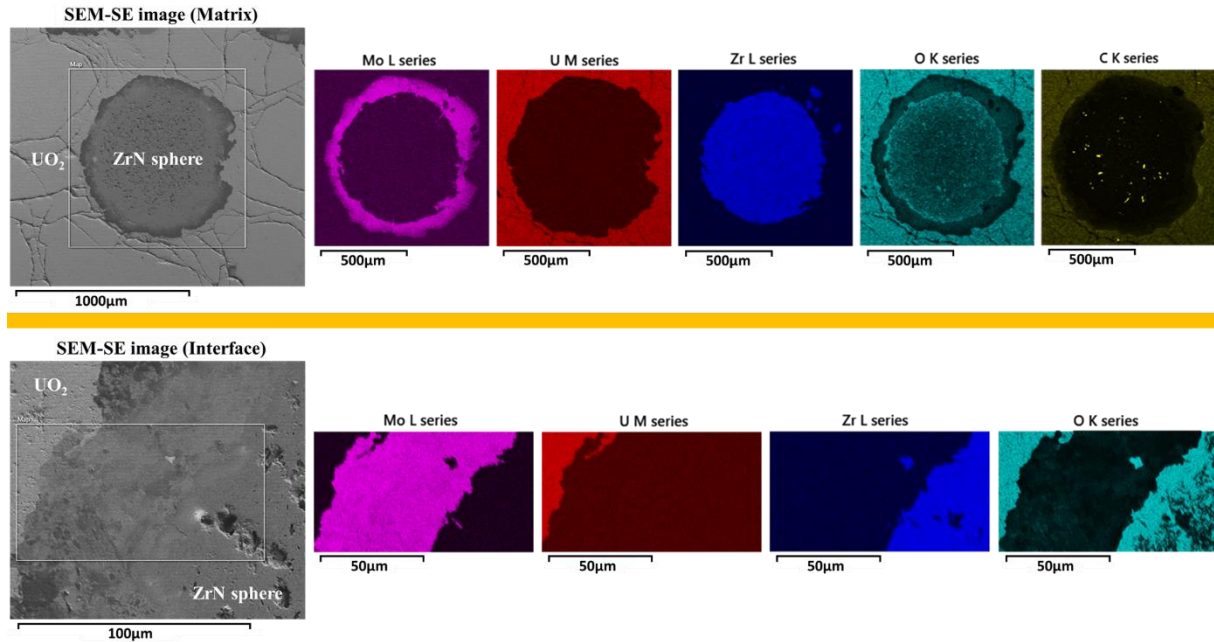


**Fig. 9.** SEM-EDS images of the Mo(binder)/ZrN-UO$_2$ composite showing a dense and thick Mo layer (~ 65 μm). This dense layer was a result of the Mo nanopowder sintering during the SPS process, as previously observed and reported [27,28,37,40].

### 3.3.3 W/ZrN-UO$_2$ composites

Fig. 10 shows the SEM images and EDS chemical maps of the W(binder)/ZrN-UO$_2$ composite matrix (top) and interface (bottom). The W map on top illustrates that the binder was essential to improve the adherence of the W nanoparticles, which was not satisfactory using only the wet method [9]. This poorer adherence of W might be due to its high density (19.3 g/cm$^3$) and because it tended to form larger agglomerates (Fig. 1). Thus, the use of a binder allowed the formation of a W coating layer of ~ 12 μm, which is thinner than that of Mo(binder)/ZrN-UO$_2$. Furthermore, no interaction between W and UO$_2$ is observed in the EDS maps of W and O at the interface. Our previous study [8] demonstrates that a W layer with a thickness of approximately 500 nm would be enough to protect the UN phase against interaction with the UO$_{2.13}$ precursor powder. This thickness is sufficient to avoid interaction during fabrication but does not consider the irradiation-induced diffusion effects.

17

Previous studies on SPS of W nanopowder demonstrate that the shrinkage starts at ~1273 K and reaches a final density greater than 95 %TD at (around) 1473 K [39,67,68,69,70]. Thus, it seems that the pre-sintered W layer, as shown in Fig. 2, achieved a density of (at least) 95 %TD after SPS at 1773 K and 80 MPa.
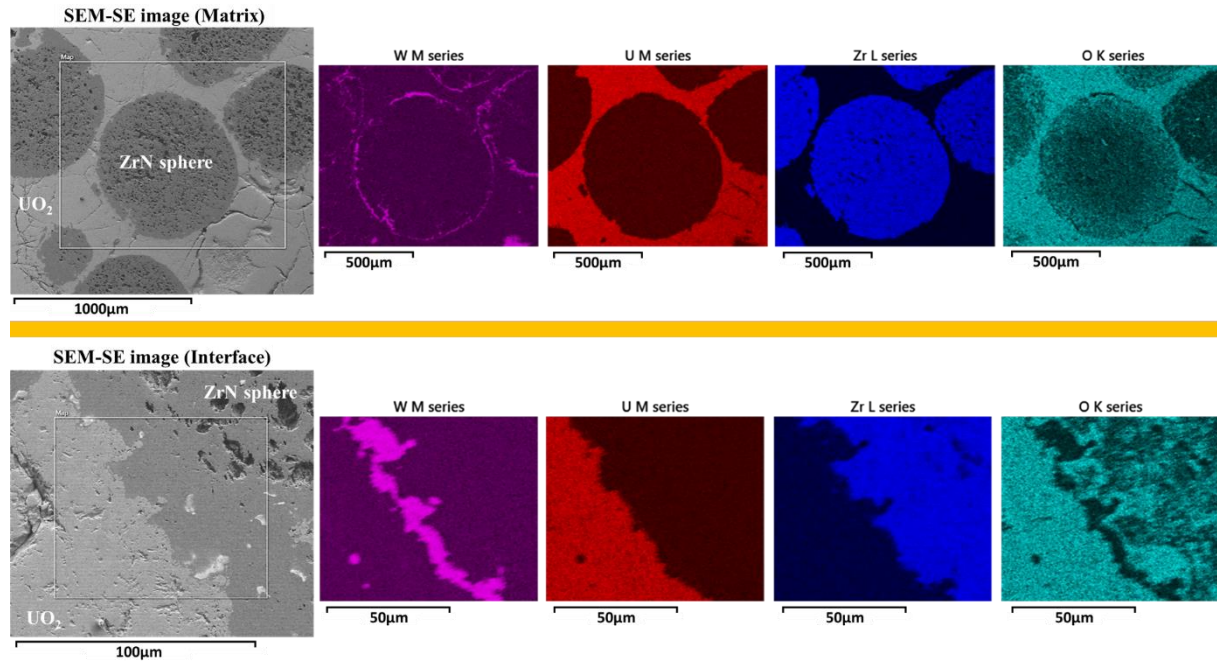


**Fig. 10.** SEM-EDS images of the W(binder)/ZrN-UO$_2$ composite. The EDS map of W (top) shows the formation of a W layer of ~ 12 μm (average), with no observable interaction between W and UO$_2$ (bottom).

The SEM-EDS results of the W(CVD)/ZrN-UO$_2$ composite in Fig. 11 (matrix) show that W was present inside the spheres. This phenomenon was due to the infiltration of WF$_6$ via open porosity and cracks in the as-fabricated ZrN spheres (Fig. 1). At the interface (bottom), a dense, pure and uniform W layer of ~3 μm with no interaction with the UO$_2$ phase is observed. This result demonstrates that the CVD-W coating (Fig. 4, Fig. 5) was dense and stable enough to keep its thickness and sharpness, even after undergoing the most severe SPS conditions (1773 K and 80 MPa) used in our previous study [6]. Thus, by using denser and smoother UN spheres (future work), we expect to obtain a dense, pure and uniform CVD-W layer covering the UN spheres. Moreover, the fine tuning of some CVD parameters (e.g. H$_2$/WF$_6$ pressure ratio) [32,34,45,48] can minimise the infiltration and trapping of fluorine in the spheres.
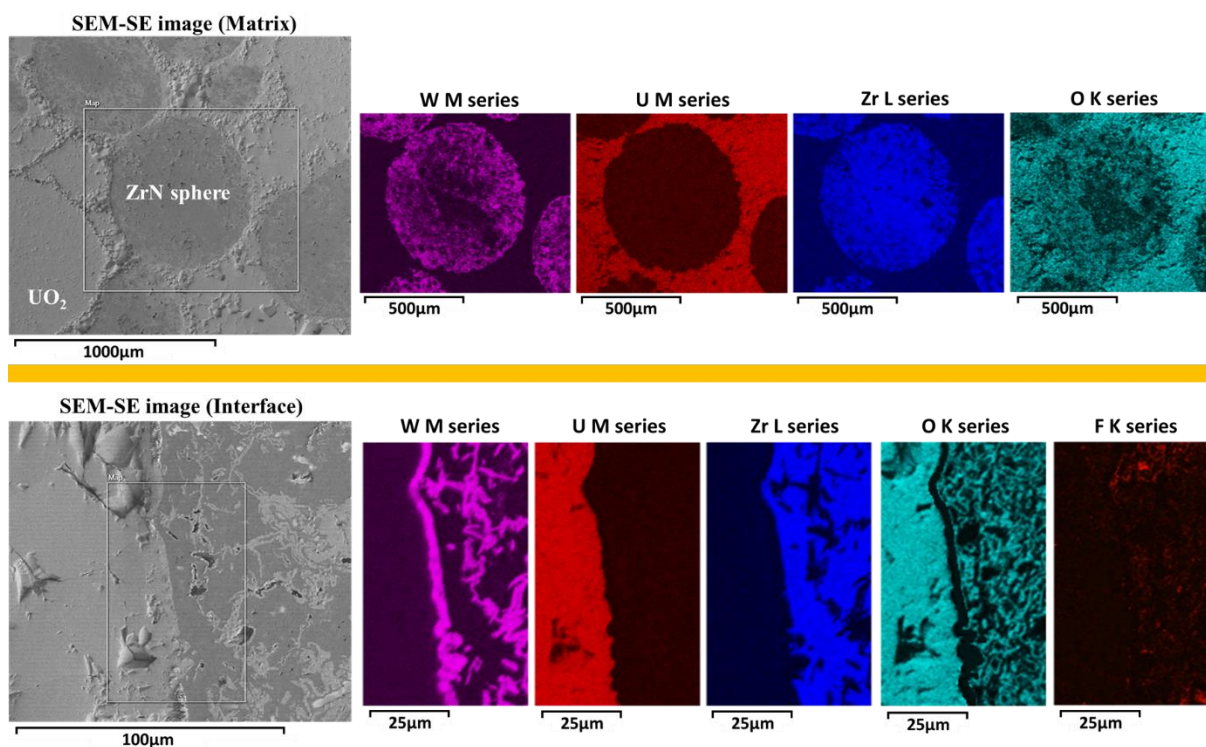
**Fig. 11.** SEM-EDS images of the W(CVD)/ZrN-UO$_2$ composite. The EDS map of W (matrix) shows that WF$_6$ infiltrated via open porosity and cracks in the as-fabricated ZrN spheres (Fig. 1). The EDS maps at the interface (bottom) report a dense, pure and uniform W layer (~ 3 µm) with no interaction with the UO$_2$ phase.

## 4. Conclusions

Coated ZrN-UO$_2$ composite fuels were successfully fabricated by SPS at 1773 K and 80 MPa. These composites are surrogates for an innovative accident tolerant fuel concept: coated UN spheres embedded in the UO$_2$ matrix. Two different coating methods were developed and studied: first, using Mo or W nanopowders (wet and binder); second, using chemical vapour deposition (CVD) of W. The SEM results of the (unmounted) coated ZrN spheres show that the external surfaces of the wet and binder methods had porous structures with particles connected by necks formed during the pre-sintering step. Conversely, the CVD technique provided a very smooth and dense external W coating layer. The EDS maps report Zr-rich regions in all (unmounted) coated samples, except in W(CVD)/ZrN.

SEM/FIB-EDS mapping of the unmounted W(CVD)/ZrN sphere shows a dense and ~3-µm thick W layer that infiltrated the available open porosity. The EDS map of F shows that fluorine was trapped in the pores and the inner region of the W layer. Similar results were

19

observed in the regular cross-section of the mounted W(CVD)/ZrN sample. Additionally, the EBSD analysis of this W layer shows polycrystalline grains with (mostly) columnar structures, average grain size of approximately 0.6 µm and no preferred crystallographic grain orientation.

Microstructural analyses of the Mo(wet)/ZrN-$UO_2$ composite reveal a cracked $UO_2$ matrix with a dense Mo layer of ~ 20µm without interaction with $UO_2$. The Mo(binder)/ZrN-$UO_2$ composite had the same matrix morphology but a dense and thicker Mo layer of ~ 65 µm. Regarding the samples coated with tungsten, the W(binder)/ZrN-$UO_2$ composite had a W layer of ~ 12 µm with no observable interaction between W and $UO_2$. The CVD technique provided a dense, pure and uniform W layer (~ 3 µm) without interaction with the $UO_2$ phase. This W layer is also observed inside the spheres since the $WF_6$ and $H_2$ reactants infiltrated via open porosity and cracks present in the as-fabricated spheres.

Thus, coated ZrN-$UO_2$ composites were successfully fabricated as surrogates for our future coated UN-$UO_2$ composite fuels. The findings in this study provide experimental results to fabricate stable UN-$UO_2$ accident tolerant fuel concepts, and may encourage further experimental and modelling developments in innovative composite fuels.

**Acknowledgments**

## References

[1] P.E. Evans, T.J. Davies, Uranium nitrides, J. Nucl. Mater. 10 (1963) 43-55, DOI: https://doi.org/10.1016/0022-3115(63)90115-6.

[2] G.A. Rama Rao, S.K. Mukerjee, V.N. Vaidya, V. Venugopal, D.D. Sood, Oxidation and hydrolysis kinetic studies on UN, J. Nucl. Mater. 185 (1991) 231-241, DOI: https://doi.org/10.1016/0022-3115(91)90340-D.

[3] S.C. Middleburgh, L. Hallstadius, M. Puide, A sintered nuclear fuel pellet, a fuel rod, a fuel assembly, and a method of manufacturing a sintered nuclear fuel pellet, Patent WO2018153572(A1) 2017, Publication Number WO/2018/153572, https://patentscope.wipo.int/search/en/detail.jsf?docId=WO2018153572.

[4] B.J. Jaques, J. Watkins, J.R. Croteau, G.A. Alanko, B. Tyburska-Püschel, M. Meyer, P. Xu, E.J. Lahoda, D.P. Butt, Synthesis and sintering of UN-$UO_2$ fuel composites, J. Nucl. Mater. 466 (2015) 745-754, DOI: https://doi.org/10.1016/j.jnucmat.2015.06.029.

[5] J.H. Yang, D.-J. Kim, K.S. Kim, Y.-H. Koo, $UO_2$-UN composites with enhanced uranium density and thermal conductivity, J. Nucl. Mater. 465 (2015) 509-515, DOI: https://doi.org/10.1016/j.jnucmat.2015.06.039.

[6] D.R. Costa, M. Hedberg, S.C. Middleburgh, J. Wallenius, P. Olsson, D.A. Lopes, UN microspheres embedded in $UO_2$ matrix: an innovative accident tolerant fuel, J. Nucl. Mater. 540 (2020) 152355, DOI: https://doi.org/10.1016/j.jnucmat.2020.152355.

[7] H. Liu, D.R. Costa, D.A. Lopes, A. Claisse, L. Messina, P. Olsson, Compatibility of UN with refractory metals (V, Nb, Ta, Cr, Mo and W): an *ab initio* approach to interface reactions and diffusion behavior, J. Nucl. Mater. 560 (2022) 153482, DOI: https://doi.org/10.1016/j.jnucmat.2021.153482.

[8] D.R. Costa, H. Liu, D.A. Lopes, S.C. Middleburgh, J. Wallenius, P. Olsson, Interface interactions in UN-X-$UO_2$ systems (X=V, Nb, Ta, Cr, Mo, W) by pressure-assisted diffusion experiments at 1773 K, J. Nucl. Mater. 561 (2022) 153554, DOI: https://doi.org/10.1016/j.jnucmat.2022.153554.

[9] D.R. Costa, M. Hedberg, H. Liu, J. Wallenius, S.C. Middleburgh, D.A. Lopes, P. Olsson, Coated UM microspheres embedded in $UO_2$ matrix as an innovative advanced technology fuel: early progress, TopFuel Conference Proceedings, Santander, Spain, 2021. ISBN: 978-92-

95064-35-5 https://www.euronuclear.org/scientific-resources/conference-proceedings/?cp=2#1559592636459-42447d8c-0fcc.

[10] M. Knez, K. Nielsch, L. Niinistö, Synthesis and surface engineering of complex nanostructures by atomic layer deposition, Adv. Mater. 19 (2007) 3425-3438, DOI: https://doi.org/10.1002/adma.200700079.

[11] D.M. King, X. Liang, Y. Zhou, C.S. Carney, L.F. Hakim, P. Li, A.W. Weimer, Atomic layer deposition of $TiO_2$ films on particles in a fluidized bed reactor, Powder Technol. 183 (2008) 356-363, DOI: https://doi.org/10.1016/j.powtec.2008.01.025.

[12] J. Elias, I. Utke, S. Yoon, M. Bechelany, A. Weidenkaff, J. Michler, L. Philippe, Electrochemical growth of ZnO nanowires on atomic layer deposition coated polystyrene sphere templates, Electrochimica Acta 110 (2013) 387-392, DOI: https://doi.org/10.1016/j.electacta.2013.04.168.

[13] P.J. Kelly, R.D. Arnell, Magnetron sputtering: a review of recent developments and applications, Vacuum 56 (2000) 159-172, DOI: https://doi.org/10.1016/S0042-207X(99)00189-X.

[14] G. Bräuer, B. Szyszka, M.Vergöhl, R. Bandorf, Magnetron sputtering – Milestones of 30 years, Vacuum 84(2010)1354-1359, DOI: https://doi.org/10.1016/j.vacuum.2009.12.014.

[15] A. Leenaers, S. Van den Berghe, C. Detavernier, Surface engineering of low enriched uranium-molybdenum, J. Nucl. Mater. 440 (2013) 220-228, DOI: https://dx.doi.org/10.1016/j.jnucmat.2013.04.068.

[16] G.H.S. Schmid, C. Eisenmenger-Sittner, A method for uniformly coating powdery substrates by magnetron sputtering, Surf. Coat. Technol. 236 (2013) 353-360, DOI: https://dx.doi.org/10.1016/j.surfcoat.2013.10.012.

[17] A.J. Johnson, R. Wilkerson, S. DiPietro, G.B. Thompson, Cermet surrogate nuclear fuels from coated powders, J. Nucl. Mater. 557 (2021) 153246, DOI: https://doi.org/10.1016/j.jnucmat.2021.153246.

[18] C. Vahlasa, B. gitte Caussat, P. Serp, G.N. Angelopoulos, Principles and applications of CVD powder technology, Mater. Scienc. Engineer. R 53 (2006) 1-72, DOI: https://doi.org/10.1016/j.mser.2006.05.001.

23

[19] Z. Cai, B. Liu, X. Zou, H.-M. Cheng, Chemical vapor deposition growth and applications of two-dimensional materials and their heterostructures, Chem. Rev. 118 (2018) 6091-6133, DOI: https://doi.org/10.1021/acs.chemrev.7b00536.

[20] L. Tang, J. Tan, H. Nong, B. Liu, H.-M. Cheng, Chemical vapor deposition growth of two-dimensional compound materials: controllability, material quality, and growth mechanism, Acc. Mater. Res. 2 (2021) 36-47, DOI: https://dx.doi.org/10.1021/accountsmr.0c00063.

[21] J. Zillinger, B. Segel, K. Benensky, D. Tucker. M. Barnes, Investigation of production parameter effects on spark plasma sintered molybdenum cermet wafers for nuclear thermal propulsion applications, Nuclear and Emerging Technologies for Space, American Nuclear Society Topical Meeting, Richland, WA, 2019, http://anstd.ans.org/.

[22] W.F. Cureton, J. Zillinger, J. Rosales, R.P. Wilkerson, M. Lang, M. Barnes, Microstructural evolution of Mo-UO$_2$ cermets under high temperature hydrogen environments, J. Nucl. Mater. 538 (2020) 152297, DOI: https://doi.org/10.1016/j.jnucmat.2020.152297.

[23] D.S. Tucker, A. O' Connor, R. Hickman, A methodology for producing uniform distribution of UO$_2$ in a tungsten matrix, J. Phys. Sc. Appl. 5 (2015) 255-262, DOI: https://doi.org/10.17265/2159-5348/2015.04.002.

[24] D.S. Tucker, M.W. Barnes, L. Hone, S. Cook, High density, uniformly distributed W/UO$_2$ for use in nuclear thermal propulsion, J. Nucl. Mater. 486 (2017) 246-249, DOI: http://dx.doi.org/10.1016/j.jnucmat.2017.01.033.

[25] D.R. Costa, M. Hedberg, S.C. Middleburgh, J. Wallenius, P. Olsson, D.A. Lopes, Oxidation of UN/U$_2$N$_3$-UO$_2$ composites: an evaluation of UO$_2$ as an oxidation barrier for the nitride phases, J. Nucl. Mater. 544 (2021) 152700, DOI: https://doi.org/10.1016/j.jnucmat.2020.152700.

[26] M. Hedberg, M. Cologna, A. Cambriani, J. Somers, C. Ekberg, Zirconium carbonitride pellets by internal sol gel and spark plasma sintering as inert matrix fuel material, J. Nucl. Mater. 479 (2016) 137-144, DOI: https://doi.org/10.1016/j.jnucmat.2016.06.034.

[27] P. Garg, S.-J. Park, R.M. German, Effect of die compaction pressure on densification behavior of molybdenum powders, Int. J. Refract. Met. & Hard Mater. 25 (2007) 16-24, DOI: https://doi.org/10.1016/j.ijrmhm.2005.10.014.

[28] G.-S. Kim, H.G. Kim, D.-G. Kim, S.-T. Oh, M.-J. Suk, Y.D. Kim, Densification behavior of Mo nanopowders prepared by mechanochemical processing, J. Alloy. Comp. 469 (2009) 401-405, DOI: https://doi.org/10.1016/j.jallcom.2008.01.149.

[29] R.M. German, Sintering: from Empirical Observations to Scientific Principles, (first ed.), Butterworth-Heinemann, Oxford (2014), ISBN: 978-0-12-401682-8.

[30] N. Senthilnathan, A.R. Annamalai, G. Venkatachalam, Synthesis of tungsten through spark plasma and conventional sintering processes, Mater. Today: Proceedings 5 (2018) 7954-7959, DOI: https://doi.org/10.1016/j.matpr.2017.11.478.

[31] J.M. Byun, E.S. Lee, Y.J. Heo, Y.-K. Jeong, S.-T. Oh, Consolidation and properties of tungsten by spark plasma sintering and hot isostatic pressing, Int. J. Refract. Met. & Hard Mat. 99 (2021) 105602, DOI: https://doi.org/10.1016/j.ijrmhm.2021.105602.

[32] J.R. Creighton, The surface chemistry and kinetics of tungsten chemical vapor deposition and selectivity loss, Thin Solid Films 241 (1994) 310-317, DOI: https://doi.org/10.1016/0040-6090(94)90448-0.

[33] A.A. Zinn, Chemical Vapor Deposition of Tungsten, Chapter 3 (1994) 105-174, DOI: https://doi.org/10.1002/9783527615858.ch3.

[34] H. Gietl, J. Riesch, J.W. Coenen, T. Höschen, R. Neu, Production of tungsten-fibre reinforced tungsten composites by a novel continuous chemical vapour deposition process, Fusion Engineering and Design 146 (2019) 1426-1430, DOI: https://doi.org/10.1016/j.fusengdes.2019.02.097.

[35] O. Guillon, J. Gonzalez-Julian, B. Dargatz, T. Kessel, G. Schierning, J. Räthel, M. Herrmann, Field-assisted sintering technology/spark plasma sintering: mechanisms, materials, and technology developments, Adv. Eng. Mater. (2014), DOI: https://doi.org/10.1002/adem.201300409.

[36] P. Cavaliere, Spark plasma sintering of materials: advances in processing and applications, Springer Nature, Switzerland, 2019, DOI: https://doi.org/10.1007/978-3-030-05327-7.

[37] R. Ohser-Wiedemann, U. Martin, H.J. Seifert, A. Müller, Densification behaviour of pure molybdenum powder by spark plasma sintering, Int. J. Refract. Met. & Hard Mater. 28 (2010) 550-557, DOI: https://doi.org/10.1016/j.ijrmhm.2010.03.003.

[38] S. Gu, M. Qin, H. Zhang, J. Ma, X. Qu, Preparation of Mo nanopowders through hydrogen reduction of a combustion synthesized foam-like $MoO_2$ precursor, Int. J. Refract. Met. & Hard Mater. 76 (2018) 90-98, DOI: https://doi.org/10.1016/j.ijrmhm.2018.05.015.

[39] S. Deng, H. Zhao, R. Li, T. Yuan, L. Li, P. Cao, The influence of the local effect of electric current on densification of tungsten powder during spark plasma sintering, Powd. Technol. 356 (2019) 769-777, DOI: https://doi.org/10.1016/j.powtec.2019.08.108.

[40] G.-D. Sun, G.-H. Zhang, K.-C. Chou, An industrially feasible pathway for preparation of Mo nanopowder and its sintering behavior, Int. J. Refrac. Met. & Hard Mater. 84 (2019) 105039, DOI: https://doi.org/10.1016/j.ijrmhm.2019.105039.

[41] S.K. Chen, J.H. Du, G.R. Gao, Z.X. Li, Microstructure study of CVD W coating on Mo single crystal rods with <111> axial orientation by EBSD, Mater. Sc. Engineer. A 434 (2006) 95-98, DOI: https://doi.org/10.1016/j.msea.2006.07.010.

[42] J. Song, Y. Lian, Y. Lv, J. Liu, Y. Yu, X. Liu, B. Yan, Z. Chen, Z. Zhuang, X. Zhao, Y. Qi, Development of CVD-W coatings on CuCrZr and graphite substrates with a PVD intermediate layer, J. Nucl. Mater. 455 (2014) 531-536, DOI: https://dx.doi.org/10.1016/j.jnucmat.2014.08.027.

[43] Y. Lv, J. Song, Y. Lian, Y. Yu, X. Liu, Z. Zhuang, The thermal properties of high purity and fully dense tungsten produced by chemical vapor deposition, J. Nucl. Mater. 457 (2015) 317-323, DOI: http://dx.doi.org/10.1016/j.jnucmat.2014.11.095.

[44] J.I. Goldstein, D.E. Newbury, P. Echlin, D.C. Joy, C.E. Lyman, E. Lifshin, L. Sawyer, J.R. Michael, Scanning Electron Microscopy and X-Ray Microanalysis, Springer; Third edition (January 31, 2003), ISBN-13: 978-0306472923.

[45] L. Raumann, J.W. Coenen, J. Riesch, Y. Mao, D. Schwalenberg, T. Wegener, H. Gietl, T. Höschen, Ch. Linsmeier, O. Guillon, Modeling and experimental validation of a $W_f$/W-fabrication by chemical vapor deposition and infiltration, Nucl. Mater. Ener. 28 (2021) 101048, DOI: https://doi.org/10.1016/j.nme.2021.101048.

[46] M.H.A. Piro, D. Sunderland, S. Livingstone, J. Sercombe, R.W. Revie, A. Quastel, K.A. Terrani, C. Judge, 2.09 - Pellet-clad interaction behavior in zirconium alloy fuel cladding, Compreh. Nucl. Mater. 2 (2020) 248-306, DOI: https://doi.org/10.1016/B978-0-12-803581-8.09799-X.

[47] Y. Lian, X. Liu, J. Wang, F. Feng, Y. Lv, J. Song, J. Chen, Influence of surface morphology and microstructure on performance of CVD tungsten coating under fusion transient thermal loads, Appl. Surf. Sc. 390 (2016) 167-174, DOI: https://doi.org/10.1016/j.apsusc.2016.08.060.

[48] L. Raumann, J.W. Coenen, J. Riesch, Y. Mao, D. Schwalenberg, H. Gietl, C. Linsmeier, O. Guillon, Improving the W coating uniformity by a COMSOL model-based CVD parameter study for denser $W_f/W$ composites, Metals 11 (2021) 1089-1104, https://doi.org/10.3390/met11071089.

[49] T.M. Besmann, D.P. Stinton, R.A. Lowden, W.Y. Lee, Chemical Vapor Deposition (CVD) and Infiltration (CVI). In: Weimer A.W. (eds) Carbide, Nitride and Boride Materials Synthesis and Processing. Springer (1997), Dordrecht. https://doi.org/10.1007/978-94-009-0071-4_22.

[50] J.D. Murphy, A. Giannattasio, Z. Yao, C.J.D. Hetherington, P.D. Nellist, S.G. Roberts, The mechanical properties of tungsten grown by chemical vapour deposition, J. Nucl. Mater. 386-388 (2009) 583-586, DOI: https://doi.org/10.1016/j.jnucmat.2008.12.182.

[51] Y. Lian, F. Feng, J. Wang, X. Liu, J. Song, Y. Wang, Z. Chen, J. Chen, Effect of high temperature annealing on the microstructure and thermal shock resistance of tungsten coatings grown by chemical vapor deposition, J. Nucl. Mater. 513 (2019) 241-250, DOI: https://doi.org/10.1016/j.jnucmat.2018.11.006.

[52] K. Sugiyama, K. Kinbara, H. Itoh, Effects of acoustic wave irradiation on chemical vapour deposition, Thin Solid Films 112 (1984) 257-266, DOI: https://doi.org/10.1016/0040-6090(84)90216-5.

[53] D.W. Woodruff, J.M. Redwing, Chemical vapor deposition of fine-grained equiaxed tungsten films, Surf. Coat. Technol. 49 (1991) 215-220, DOI: https://doi.org/10.1016/0257-8972(91)90058-5.

[54] T. Zweifel, H. Palancher, A. Leenaers, A. Bonnin, V. Honkimaki, R. Tucoulou, S. Van Den Berghe, R. Jungwirth, F. Charollais, W. Petry, Crystallographic study of Si and ZrN coated U-Mo atomised particles and of their interaction with Al under thermal annealing, J. Nucl. Mater. 442 (2013) 124-132, DOI: https://dx.doi.org/10.1016/j.jnucmat.2013.08.050.

27

[55] R. Jungwirth, T. Zweifel, H.-Y. Chiang, W. Petry, S. Van den Berghe, A. Leenaers, Heavy ion irradiation of UMo/Al samples PVD coated with Si and ZrN layers, J. Nucl. Mater. 434 (2013) 296-302, DOI: https://dx.doi.org/10.1016/j.jnucmat.2012.11.032.

[56] F. Housaer, F. Vanni, M. Touzin, F. Béclin, J. Allenou, A. Leenaers, A.M. Yacout, H. Palancher, B. Stepnik, O. Tougait, Morphological characterization of the fresh ZrN coated UMo powders used in EMPIrE irradiation experiment: A practical approach, J. Nucl. Mater. 533 (2020) 152087, DOI: https://doi.org/10.1016/j.jnucmat.2020.152087.

[57] J.-H. Huang, K.-L. Kuo, G.-P. Yu, Oxidation behavior and corrosion resistance of vacuum annealed ZrN-coated stainless steel, Surf. & Coat. Techn. 358 (2019) 308-319, DOI: https://doi.org/10.1016/j.surfcoat.2018.11.054.

[58] D. Jianxin, L. Jianhua, Z. Jinlong, S. Wenlong, Wear mechanisms of PVD ZrN coated tools in machining, Int. J. Refract. Met. & Hard Mater. 26 (2008) 164-172, DOI: https://doi.org/10.1016/j.ijrmhm.2007.05.009.

[59] A. Leenaers, B. Ye, J. Van Eyken, S. Van den Berghe, ZrN coating as diffusion barrier in U(Mo) dispersion fuel systems, J. Nucl. Mater. 552 (2021) 153000, DOI: https://doi.org/10.1016/j.jnucmat.2021.153000.

[60] C.B. Barry, N.M. Grant, Ceramic Materials Science and Engineering, Springer, 2007, ISBN: 0387462708.

[61] J.K. Fink, Thermophysical properties of uranium dioxide, J. Nucl. Mater. 279 (2000) 1-18, DOI: https://doi.org/10.1016/S0022-3115(99)00273-1.

[62] K. Aigner, W. Lengauer, D. Rafaja, P. Ettmayer, Lattice parameters and thermal expansion of $Ti(C_xN_{1-x})$, $Zr(C_xN_{1-x})$, $Hf(C_xN_{1-x})$ and $TiN_{1-x}$ from 298 to 1473 K as investigated by high-temperature X-ray diffraction, J. Alloys Comp. 215 (1994) 121-126, DOI: https://doi.org/10.1016/0925-8388(94)90828-1.

[63] K. Wang, R.R. Reeber, The role of defects on thermophysical properties: thermal expansion of V, Nb, Ta, Mo and W, Mater. Sci. Engin. 23 (1998) 101-137, https://doi.org/10.1016/S0927-796X(98)00011-4.

[64] D.-J. Kim, Y.W. Rhee, J.H. Kim, K.S. Kim, J.S. Oh, J.H. Yang, Y.-H. Koo, K.-W. Song, Fabrication of micro-cell $UO_2$–Mo pellet with enhanced thermal conductivity, J. Nucl. Mater. 462 (2015) 289-295, DOI: http://dx.doi.org/10.1016/j.jnucmat.2015.04.003.

[65] L. Cheng, R. Gao, B. Yan, C. Zhang, R. Li, C. Ma, Z. Yang, B. Li, Y. Wang, Y. Zhong, M. Chu, B. Bai, P. Zhang, Investigation of the residual stress in $UO_2$-Mo composites via a neutron diffraction method, Ceram. Internat. 46 (2020) 15889-15896, DOI: https://doi.org/10.1016/j.ceramint.2020.03.137.

[66] M.K. Tummalapalli, J.A. Szpunar, A. Prasad, L. Bichler, EBSD studies on microstructure and crystallographic orientation of $UO_2$-Mo composite fuels, Nucl. Engineer. Technol. 53 (2021) 4052-4059, DOI: https://doi.org/10.1016/j.net.2021.06.028.

[67] J. Matějíček, J. Veverka, C. Yin, M. Vilémová, D. Terentyev, M. Wirtz, M. Gago, A. Dubinko, H. Hadraba, Spark plasma sintered tungsten - mechanical properties, irradiation effects and thermal shock performance, J. Nucl. Mater. 542 (2020) 152518, DOI: https://doi.org/10.1016/j.jnucmat.2020.152518.

[68] S. Deng, H. Zhao, R. Li, T. Yuan, L. Li, P. Cao, The influence of the local effect of electric current on densification of tungsten powder during spark plasma sintering, Powd. Techn. 356 (2019) 769-777, DOI: https://doi.org/10.1016/j.powtec.2019.08.108.

[69] H.C. Kim, E. Bang, N. Kwak, Y. Oh, H.N. Han, H. Choi, K. Kim, S.-H. Hong, Thermal and microstructural properties of spark plasma sintered tungsten for the application to plasma facing materials, Fusion Engineer. Design 146 (2019) 2649-2653, DOI: https://doi.org/10.1016/j.fusengdes.2019.04.071.

[70] J. Choi, H.-M. Sung, K.-B. Roh, S.-H. Hong, G.-H. Kim, H.N. Han, Fabrication of sintered tungsten by spark plasma sintering and investigation of thermal stability, Intern. J. Refract. Met. & Hard Mater. 69 (2017) 164-169, DOI: http://dx.doi.org/10.1016/j.ijrmhm.2017.08.013.